

1 **Seasonality in Arctic Warming Driven By Sea Ice Effective Heat Capacity**

2 Lily C. Hahn^a, Kyle C. Armour^{a,b}, David S. Battisti^a, Ian Eisenman^c, Cecilia M. Bitz^a

3 ^a*Department of Atmospheric Sciences, University of Washington, Seattle, WA*

4 ^b*School of Oceanography, University of Washington, Seattle, WA*

5 ^c*Scripps Institution of Oceanography, University of California San Diego, La Jolla, CA*

6

7 *Corresponding author: Lily C. Hahn, lchahn@uw.edu*

8
9
10
11
12
13
14
15
16
17
18
19
20
21
22
23
24
25
26
27
28
29
30
31

ABSTRACT

Arctic surface warming under greenhouse gas forcing peaks in early winter and reaches its minimum during summer in both observations and model projections. Many mechanisms have been proposed to explain this seasonal asymmetry, but disentangling these processes remains a challenge in the interpretation of general circulation model (GCM) experiments. To isolate these mechanisms, we use an idealized single-column sea ice model (SCM) which captures the seasonal pattern of Arctic warming. SCM experiments demonstrate that as sea ice melts and exposes open ocean, the accompanying increase in effective surface heat capacity can alone produce the observed pattern of peak early winter warming by slowing the seasonal heating and cooling rate, thus delaying the phase and reducing the amplitude of the seasonal cycle of surface temperature. To investigate warming seasonality in more complex models, we perform GCM experiments that individually isolate sea-ice albedo and thermodynamic effects under CO₂ forcing. These also show a key role for the effective heat capacity of sea ice in promoting seasonal asymmetry through suppressing summer warming, in addition to precluding summer climatological inversions and a positive summer lapse-rate feedback. Peak winter warming in GCM experiments is further supported by a positive winter lapse-rate feedback that persists with only the albedo effects of sea-ice loss prescribed, due to cold initial surface temperatures and strong surface-trapped warming. While many factors support peak early winter warming as Arctic sea ice declines, these results highlight changes in effective surface heat capacity as a central mechanism contributing to this seasonality.

32

PLAIN LANGUAGE SIGNIFICANCE STATEMENT

33 Under increasing concentrations of atmospheric greenhouse gases, the strongest
34 Arctic warming occurs during early winter, but the reasons for this seasonal pattern of
35 warming are not well understood. We use experiments in both simple and complex models
36 with certain sea-ice processes turned on and off to disentangle potential drivers of the early
37 winter peak in Arctic warming. When sea ice melts and open ocean is exposed, surface
38 temperatures are slower to reach the warm-season maximum and slower to cool back down
39 below freezing in early winter. We find that this process alone can produce the observed
40 pattern of maximum Arctic warming in early winter, highlighting a fundamental mechanism
41 for the seasonal pattern of Arctic warming.

42 **1. Introduction**

43 In both observations and model simulations, recent Arctic surface warming has
44 outpaced the global average by a factor of more than two (Screen and Simmonds, 2010a;
45 Serreze et al., 2009). While sea-ice melt and the ice-albedo feedback peak during summer,
46 the strongest Arctic warming is observed several months later during early winter (Screen
47 and Simmonds, 2010b). This seasonal asymmetry is also found in model projections, from
48 the earliest model generations to the newest iteration of climate models in the Coupled Model
49 Intercomparison Project phase 6 (CMIP6) (Deser et al., 2010; Hahn et al., 2021; Holland and
50 Bitz, 2003; Manabe and Stouffer, 1980). Figure 1 illustrates the seasonal pattern of Arctic
51 warming within the fully-coupled Community Earth System Model version 2 (CESM2)
52 (Danabasoglu et al., 2020). While consistent with other CMIP6 models in producing winter-
53 amplified Arctic warming, this model's inclusion of a *IpctCO2-4xext* experiment illustrates a
54 full range of annually ice-covered, seasonally ice-free, and annually ice-free conditions. In
55 this experiment, a 1%-per-year increase in atmospheric CO₂ is applied up to a quadrupling of

56 pre-industrial concentrations in year 140, with constant CO₂ forcing thereafter. The evolving
57 seasonal cycle of near-surface air temperature (TAS) area-averaged over non-land surfaces
58 from 70-90°N in this experiment (Figure 1a) and the change in TAS with respect to a pre-
59 industrial control (*piControl*) experiment with greenhouse gas concentrations from the year
60 1850 (Figure 1b) show several key features: (i) stronger warming during winter than summer;
61 (ii) peak warming in early winter for the first 150 years of the experiment; and (iii) a shift to
62 peak warming in late winter for higher global warming levels later in the experiment, once
63 early winter temperatures exceed the freezing point. While these features suggest that sea-ice
64 loss plays a key role in setting the seasonal pattern of near-surface Arctic warming, they raise
65 the question of how this pattern is produced.

66 Commonly proposed mechanisms linking sea-ice loss to seasonal asymmetry in
67 Arctic warming include: (i) the delayed warming effect, in which increased surface solar
68 absorption due to reduced summer ice cover contributes to seasonal ocean heat storage and its
69 release to the atmosphere in winter; and (ii) the ice insulation effect, in which reduced sea-ice
70 thickness and extent allows for stronger heat transfer from the relatively warm upper ocean to
71 the colder atmosphere above particularly during winter, when the air-sea temperature
72 difference is greatest (Deser et al., 2010; Manabe and Stouffer, 1980; Screen and Simmonds,
73 2010b). Seasonality in Arctic warming has also been attributed to longwave cloud and
74 temperature feedbacks, including the lapse-rate and Planck feedbacks (Bintanja and van der
75 Linden 2013; Lu and Cai, 2009; Pithan and Mauritsen, 2014; Sejas et al., 2014; Yoshimori et
76 al., 2014). A positive winter lapse-rate feedback in the Arctic results from surface-trapped
77 warming which produces weaker longwave emission to space than a vertically uniform
78 atmospheric warming. As this surface-trapped warming is supported by a stable lower
79 troposphere that inhibits vertical mixing, stronger stability in winter promotes a winter-

80 peaking Arctic lapse-rate feedback (Cronin and Jansen, 2015; Hahn et al., 2020; Payne et al.,
81 2015). Seasonality in the Planck feedback would also contribute to greater warming in winter
82 than in summer due to a weaker increase in outgoing longwave radiation for a surface
83 warming at initially colder temperatures (Pithan and Mauritsen, 2014).

84 Many of these mechanisms are interconnected, making it difficult to distinguish their
85 relative importance for seasonality in Arctic warming. After seasonal ocean heat storage, the
86 lapse-rate feedback is the second largest contributor to seasonal asymmetry in Arctic
87 warming for models in the Coupled Model Intercomparison Project phase 5 and 6 (Hahn et
88 al., 2021; Pithan and Mauritsen, 2014). Bintanja et al. (2011) and Hahn et al. (2020) suggest
89 that the polar lapse-rate feedback depends on the base-state inversion strength, which itself
90 depends on the existence of sea ice, poleward atmospheric heat transport, and atmospheric
91 emissivity (Cronin and Jansen, 2015; Payne et al., 2015; Pithan et al., 2014). More recently,
92 Boeke et al. (2021) find that while inversions are necessary for a positive lapse-rate feedback,
93 this feedback depends more strongly on the amount of surface warming than on the degree of
94 stable stratification. As a result, a more-positive lapse-rate feedback in winter could result
95 from any process that promotes stronger bottom-heavy atmospheric warming, including the
96 ice-albedo feedback (Feldl et al., 2017; Graversen et al., 2014). Dai et al. (2019) and Chung
97 et al. (2021) further suggest that seasonal ocean heat storage and sea-ice insulation loss are
98 necessary to kickstart the winter lapse-rate feedback via increased turbulent heat release to
99 the atmosphere over newly opened ocean. Separating these potentially interdependent ice-
100 albedo, seasonal ocean heat storage, and insulation effects of sea-ice loss and their impact on
101 the lapse-rate feedback remains a challenge in comprehensive climate models.

102 An additional mechanism for winter-amplified warming that has received less
103 attention is the role of changes in the effective heat capacity of the surface layer in the Arctic.

104 As in Dwyer et al. (2012), here we use the term “effective heat capacity” to refer to the
105 thermal inertia of the layer of material (e.g., sea ice, ocean) that sets the surface temperature
106 response to surface heat fluxes. Turbulent mixing in the ocean mixed layer couples a thick
107 layer of water to surface heat fluxes, giving the surface ocean a relatively large effective heat
108 capacity. As a result, ocean surface temperatures respond slowly to surface heat fluxes and
109 with a smaller amplitude than temperatures over land, where a much thinner surface layer
110 responds more quickly and strongly. Meanwhile, the effective heat capacity of sea ice
111 depends on whether it is melting or at temperatures below freezing. At the melting point, sea
112 ice has a large effective heat capacity because surface heat fluxes go toward latent heating to
113 melt ice rather than raising the surface temperature; melting sea ice thus acts like a very deep
114 ocean mixed layer. However, frozen sea ice has a small effective heat capacity because
115 surface heat fluxes go directly toward changing its surface temperature; frozen sea ice acts
116 like a shallow ocean mixed layer or a land-like surface. As frozen sea ice warms to the
117 melting point and then, ultimately, melts completely to expose open ocean, the effective heat
118 capacity of the surface increases. This slows the seasonal rate of warming and cooling and
119 thereby delays the phase and reduces the amplitude of the seasonal cycle of surface
120 temperature. As shown in Dwyer et al. (2012) for CMIP3 models, this phase delay and
121 amplitude reduction has also been found in earlier model generations (Manabe and Stouffer,
122 1980; Mann and Park, 1996) and is consistent with the warming pattern shown in Figure 1.
123 For a doubling of CO₂, the large effective heat capacity of melting ice suppresses summer
124 warming, supporting a winter warming maximum. Under increased forcing, the amplitude
125 reduction from frozen sea ice to open ocean supports a large difference between very cold
126 winters over ice and warmer winters over ocean, contributing to peak winter warming. Peak
127 warming specifically in early winter is supported by the phase delay in ocean temperatures,
128 which are slower to warm to the seasonal maximum and to cool back below freezing. As a

129 result, the transition from frozen sea ice to open ocean under increased forcing and the
130 accompanying warming maximum occurs first in early winter before shifting to late winter.

131 The changes in surface effective heat capacity described above are one of several
132 potential explanations for seasonality in Arctic warming that have been generated by
133 diagnostic analysis of CO₂ forcing experiments in comprehensive general circulation models
134 (GCMs). To disentangle these interconnected effects of sea-ice loss, here we employ an
135 idealized single-column sea ice model (SCM) in addition to a GCM with certain sea-ice
136 processes turned on and off. SCM experiments enable us to separate drivers of seasonality in
137 Arctic warming, particularly the role of effective heat capacity changes alone, while GCM
138 experiments offer insight into additional processes not included in the SCM, such as the
139 lapse-rate feedback. Complementary to previous studies that have isolated the albedo effects
140 of sea ice using experiments with locked or unlocked albedo changes (Feldl et al., 2017;
141 Graversen et al., 2014), we isolate the role of non-albedo sea-ice thermodynamics by
142 comparing experiments with identical surface albedo changes, but with sea ice turned on or
143 off. Both the simple SCM and more complex GCM reveal a fundamental role of increasing
144 effective heat capacity in producing seasonality in Arctic warming, as the surface layer shifts
145 from sea ice below the freezing point to melting ice and open ocean. The results also
146 highlight the role of sea ice effective heat capacity for inhibiting a positive summertime
147 lapse-rate feedback, which additionally supports a winter warming maximum.

148 **2. Seasonal Asymmetry in a Single-Column Sea Ice Model**

149 *a. Model description*

150 We employ an idealized SCM of the sea-ice–ocean–atmosphere system to investigate
151 different mechanisms that have been proposed to cause seasonality in Arctic warming. We
152 use the SCM developed and described by Eisenman and Wettlaufer (2009), which includes an

153 idealized version of the Maykut and Untersteiner (1971) sea-ice thermodynamic equations
 154 and an idealized atmosphere. The SCM equations are repeated below. This model evolves the
 155 surface enthalpy E , which represents the latent energy of sea ice or, when no ice is present,
 156 the sensible energy of the ocean mixed layer:

$$157 \quad E = \begin{cases} -L_i H_i, & E < 0 \text{ (sea ice)} \\ c_{ml} H_{ml} T_{ml}, & E > 0 \text{ (ocean)} \end{cases}, \quad (1)$$

158 where L_i is the latent heat of fusion for sea ice, H_i is the sea-ice thickness, c_{ml} is the specific
 159 heat capacity of the ocean mixed layer, H_{ml} is depth of the ocean mixed layer (50 m), and T_{ml}
 160 is the mixed-layer temperature departure from the freezing point, which is 0°C in this model.
 161 E evolves in response to the net surface energy flux, which includes solar forcing as a
 162 function of the insolation $F_s(t)$ and surface albedo $\alpha(E)$, a linearized representation of
 163 outgoing longwave radiation (OLR), basal heat flux F_B , sea ice export, and climate forcing
 164 ΔF_0 , which can be varied from 0 to represent an increase in atmospheric CO_2 :

$$165 \quad \frac{dE}{dt} = \underbrace{[1 - \alpha(E)]F_s(t)}_{\text{solar}} - \underbrace{F_0(t) - F_T(t)T(t, E)}_{\text{OLR}} + \underbrace{F_B}_{\text{basal heat flux}} + \underbrace{v_o R(-E)}_{\text{ice export}} + \underbrace{\Delta F_0}_{\text{forcing}}. \quad (2)$$

166 The prescribed values of $F_s(t)$, $F_0(t)$, and $F_T(t)$ vary seasonally, while F_B and ΔF_0 are
 167 annually constant. $F_0(t)$ and $F_T(t)$ values have been derived as a function of atmospheric
 168 opacity, including the effects of climatological Arctic cloud cover (Maykut and Church,
 169 1973), and atmospheric heat transport to the Arctic, which is based on observations of surface
 170 air temperature to the south of the Arctic (Kalnay et al., 1996; Nakamura and Oort, 1988).
 171 Central Arctic values from Maykut and Untersteiner (1971) are prescribed for $F_s(t)$ and F_B .
 172 In the ice export term, $v_o = 10\% \text{ year}^{-1}$, and the linear ramp function $R(-E)$ is equal to $-E$
 173 when ice is present ($E \leq 0$) and zero when there is no ice ($E > 0$).

174 When ice is present, the surface temperature T is calculated using a balance between
 175 the surface energy flux and the upward heat flux through the ice: $-[1 - \alpha(E)]F_s(t) +$
 176 $F_0(t) + F_T(t)T^*(t, E) - \Delta F_0 = \frac{-k_i T^*(t, E)}{H_i} = \frac{k_i L_i T^*(t, E)}{E}$, where k_i is the thermal conductivity
 177 of sea ice and T^* is the surface temperature satisfying this balance. When this balance gives
 178 surface temperatures below freezing ($T^* < 0$), T is set to T^* . When this balance gives surface
 179 temperatures above freezing ($T^* > 0$) while ice is still present ($E < 0$), T is fixed at the
 180 freezing point (0°C) while the ice melts. Once the ocean is ice-free ($E > 0$), T equals the
 181 enthalpy of the mixed layer divided by its effective heat capacity. The surface temperature for
 182 these three regimes is given by

$$183 \quad T(t, E) = \begin{cases} -\frac{(1-\alpha_i)F_s(t) - F_0(t) + \Delta F_0}{k_i L_i / E - F_T(t)}, & E < 0, T^* < 0 \text{ (frozen ice)}, \\ 0, & E < 0, T^* > 0 \text{ (melting ice)}, \\ \frac{E}{c_{ml} H_{ml}}, & E \geq 0 \text{ (open ocean)}. \end{cases} \quad (3)$$

184
 185 The albedo $\alpha(E)$ transitions smoothly from ice ($\alpha_i = 0.68$) to ocean ($\alpha_{ml} = 0.2$) with
 186 a characteristic smoothness set by $H_\alpha = 0.5$ m:

$$187 \quad \alpha(E) = \frac{\alpha_{ml} + \alpha_i}{2} + \frac{\alpha_{ml} - \alpha_i}{2} \tanh\left(\frac{E}{L_i H_\alpha}\right). \quad (4)$$

188 *b. Seasonal pattern of warming in the SCM*

189 To assess the extent to which this simple model can reproduce the pattern of
 190 seasonality in Arctic warming found in more complex models and observations, we compare
 191 steady-state solutions under varying degrees of forcing in the SCM with CESM2 pre-
 192 industrial control and *IpctCO2-4xext* experiments (Figure 2a,b). These CESM2 experiments
 193 are identical to those displayed in Figure 1, but Figure 2a shows surface temperature for 90°N
 194 rather than near-surface temperature for $70\text{-}90^\circ\text{N}$ for better comparison with the SCM, which

195 models surface temperature using observationally-based parameters for the central Arctic.
196 The bottom row in Figure 2 shows surface temperature anomalies for climate forcing
197 experiments with respect to experiments with pre-industrial CO₂ (for CESM2) or $\Delta F_0 = 0$ (for
198 the SCM).

199 The SCM experiment with $\Delta F_0 = 0$ produces a similar seasonal cycle to CESM2
200 under pre-industrial forcing. Greater climate forcing is required to produce a given warming
201 in the SCM because it excludes many of the climate feedbacks in CESM2; rather than show
202 equivalent forcings for both models, we include forcings that illustrate the full range of
203 responses: annually ice-covered, seasonally ice-free, and annually ice-free conditions.
204 Despite neglecting many processes that additionally impact surface temperature, the SCM
205 captures the key features of seasonality in Arctic warming found in CESM2. This includes (i)
206 enhanced warming in winter compared to summer, (ii) asymmetry in winter warming, with
207 peak warming initially occurring in early winter, and (iii) a shift to peak warming in late
208 winter with greater forcing, once early winter temperatures exceed the freezing point. This
209 warming pattern can also be described as a phase delay and amplitude reduction in the
210 surface temperature as the surface layer shifts from perennial sea ice cover to seasonally and
211 annually ice-free conditions.

212 *c. Causes of seasonal warming asymmetry in the SCM*

213 With the SCM capturing the seasonal pattern of Arctic warming found in observations
214 and more complex models, we next investigate factors contributing to this pattern in this
215 model. The SCM includes a representation of several mechanisms that have been suggested
216 to contribute to seasonality in Arctic warming: seasonally varying Planck and surface-albedo
217 feedbacks; changes in ice insulation and conductive heat flux as sea ice thins; and changes in
218 surface effective heat capacity as sea ice melts and exposes open ocean. Lapse-rate, cloud,

219 and water-vapor feedbacks and changes in poleward heat transport are not included in the
220 SCM, but are later explored in GCM experiments (Section 3) and by incorporating a lapse-
221 rate feedback parameterization into the SCM (Section 2f).

222 The surface-albedo and Planck feedbacks both contribute to seasonal warming
223 asymmetry in the SCM. Enthalpy maximizes at the end of summer and increases most at this
224 time under forcing, yielding a late summer maximum in the positive albedo feedback. The
225 Planck feedback, equal to $-F_T(t)$ in the SCM, is a function of observations of climatological
226 Arctic cloud fraction (Maykut and Church, 1973) which reach a maximum in September,
227 producing a less-negative Planck feedback in fall and early winter than in late winter. While
228 nonlinearity in the Stefan-Boltzmann equation would also promote seasonality in the Planck
229 feedback and amplify cold-season warming in GCMs, the linearized Planck response in the
230 SCM contributes to seasonality in warming only as a result of seasonality in climatological
231 atmospheric opacity. The early winter warming maximum in the SCM is dampened when
232 either an annual-mean Planck feedback ($\overline{F_T}$) or constant ice albedo ($\alpha(E) = \alpha_i$) is
233 implemented (Figure S1), with the combined influence of these changes shown in Figure 2c.
234 Comparison of Figure 2b and 2c illustrates that the seasonally varying Planck feedback and
235 particularly the albedo feedback reduce the amount of forcing necessary to support a
236 transition to open ocean in early winter and an associated increase in early winter warming.
237 However, seasonal asymmetry in warming persists even in the absence of seasonal
238 asymmetry in feedbacks (Figure 2c), suggesting that the warming maximum in early winter
239 (and in late winter under increased forcing) is a fundamental property of warming with sea-
240 ice loss.

241 We next explore seasonality in warming contributed by changes in the conductive
242 heat flux through sea ice ($\frac{-k_i T}{H_i}$), which maximizes in early winter as a result of both thinner

243 ice and colder surface temperatures, and increases with increased forcing as ice thins. To
244 illustrate the effects of seasonality in conductive heat flux and its increase with forcing, we
245 compare the SCM with an annual-mean Planck feedback and constant ice albedo ($\overline{F_T}$ and
246 $\alpha(E) = \alpha_i$; see Figure 2c) to the same SCM, but with a constant ice thickness H_i used when
247 calculating the conductive heat flux through frozen ice (Figure 2d). This constant H_i is set to
248 the annual-mean ice thickness from the $\Delta F_0 = 0$ experiment with $\overline{F_T}$ and $\alpha(E) = \alpha_i$. With
249 constant ice thickness in the conductive heat flux, warming for a given forcing is identical in
250 all months with frozen ice (Figure 2d). This illustrates that seasonally varying ice depth in the
251 conductive heat flux contributes to peak warming in early winter over frozen ice (Figure 2c).
252 Increasing conductive heat flux through thinner ice enhances surface warming in winter as
253 the surface forcing increases. In addition to enhanced warming over frozen ice, winter
254 warming as ice transitions to open ocean is also strengthened by starting from very cold
255 surface temperatures as a result of limited conductive heat flux through thick ice; this
256 warming is weakened when a thinner base-state ice depth is prescribed in the conductive heat
257 flux (Figure S2). The dependence of conductive heat flux on sea ice thickness thus
258 contributes to greater winter warming both over frozen ice and for the transition to open
259 ocean.

260 Importantly, even with seasonally constant warming over frozen ice in Figure 2d, the
261 transition from frozen ice to seasonally ice-free ocean with increased forcing produces an
262 early winter warming maximum, and the transition from seasonally to annually ice-free
263 conditions produces a late winter warming maximum. This intrinsic link between the ice-
264 ocean transition and peak Arctic warming, even in the absence of seasonal variations in
265 feedbacks or insulation effects, suggests that the seasonal pattern of warming fundamentally
266 stems from changes in the effective heat capacity of these surface types (Dwyer et al., 2012;

267 Manabe & Stouffer, 1980; Mann and Park, 1996). As frozen sea ice transitions to open ocean
 268 in fall and early winter with increased forcing, the greater effective heat capacity of the ocean
 269 mixed layer slows seasonal warming in summer and slows cooling back below freezing in
 270 early winter, supporting a large increase in early winter temperatures relative to the much
 271 colder temperatures of frozen ice under control forcing.

272 *d. Contribution of effective heat capacity changes to the seasonal pattern of Arctic warming*

273 We further investigate the role of effective heat capacity for seasonality in Arctic
 274 warming by explicitly modelling effective heat capacity changes in the SCM, and compare
 275 the results with an analytical solution based on Dwyer et al. (2012). Dwyer et al. illustrate
 276 heat capacity effects on seasonality using a simple energy balance model,

$$277 \quad C \frac{dT}{dt} = Q(t) - \beta T(t) , \quad (5)$$

278 where C is effective heat capacity, $T(t)$ is surface temperature, $Q(t)$ is the seasonally varying
 279 surface forcing independent of temperature (including solar forcing), and β is a constant, with
 280 $-\beta T(t)$ representing damping of the surface temperature response (including through OLR
 281 changes). This gives the following phase and amplitude relationships between the surface
 282 forcing, $Q(t) = Q_o \cos(\omega t - \phi_Q)$, and the surface temperature, $T(t) = T_o \cos(\omega t - \phi_T)$,
 283 with $\omega = 2\pi \text{ yr}^{-1}$:

$$284 \quad \phi_T - \phi_Q = \arctan \frac{\omega C}{\beta} , \quad (6)$$

$$285 \quad T_o = \frac{Q_o}{\sqrt{\beta^2 + \omega^2 C^2}} . \quad (7)$$

286 In the limit of small effective heat capacity ($C \rightarrow 0$), there is no phase lag between $Q(t)$ and
 287 surface temperature, while a much larger effective heat capacity ($C \rightarrow \infty$) gives a maximum
 288 phase delay of 90° , or three months for an annual harmonic forcing. A transition from frozen

289 ice to open ocean with increased forcing would cause an increase in effective heat capacity
290 and thus a phase delay (Eq. 6) and amplitude reduction (Eq. 7) in surface temperature,
291 consistent with the SCM response in Figure 2d.

292 To explicitly model the effect of heat capacity differences between frozen ice, melting
293 ice, and open ocean, we run the SCM as an ocean mixed layer, the effective heat capacity of
294 which can be modified by changing the mixed layer depth ($C = c_{ml}H_{ml}$). Without sea ice in
295 this version of the model, Eq. 3 becomes $T(t, E) = \frac{E}{c_{ml}H_{ml}}$, ice export is set to zero, and
296 there is no conductive heat flux. As above, we also apply an annual-mean Planck feedback
297 and constant ice albedo ($\overline{F_T}$ and $\alpha(E) = \alpha_i$) in order to isolate the impact of heat capacity
298 changes alone on seasonality in Arctic warming. We perform four sets of experiments with
299 this SCM: (i) using a mixed layer depth of $H_{ml} = 1$ m (representing the small effective heat
300 capacity of frozen ice); (ii) using a mixed layer depth of $H_{ml} = 50$ m (representing the large
301 effective heat capacity of open ocean); (iii) using a variable mixed layer depth that is $H_{ml} = 1$
302 m when the surface temperature is below freezing, defined by $E < 0$ (representing the small
303 effective heat capacity of frozen ice) and becomes $H_{ml} = 50$ m when the surface temperature
304 is at or above the melting point, defined by $E \geq 0$ (representing the large effective heat
305 capacity of open ocean); and (iv), as in (iii) but using $H_{ml} = 10^6$ m when $E \geq 0$ (representing
306 the very large effective heat capacity associated with the latent energy sink of sea ice melting
307 at a nearly-constant temperature).

308 Consistent with Eq. (6) and (7), SCM experiment (ii) with a deep mixed layer
309 representing open ocean shows a delayed phase and reduced amplitude in surface temperature
310 (Figure 3b) compared to experiment (i) with a shallow mixed layer representing frozen ice
311 (Figure 3a), while both experiments show a seasonally-uniform warming in response to
312 forcing. In experiment (iii), which allows a transition from the effective heat capacity of

313 frozen ice for $E < 0$ to that of ocean when $E \geq 0$ (Figure 3c), an increase in effective heat
 314 capacity under forcing produces peak warming in early winter by delaying the phase and
 315 reducing the amplitude of surface temperature (Figure 3c). Under greater forcing, this ice-
 316 ocean transition and associated amplitude reduction from colder ice to warmer ocean
 317 temperatures occurs later in the year, producing peak warming in late winter. Similarly,
 318 experiment (iv), which allows a transition from the effective heat capacity of frozen ice for
 319 $E < 0$ to the much larger effective heat capacity of melting ice when $E \geq 0$ produces nearly
 320 identical results to experiment (iii) with an early (shifting to late) winter warming maximum
 321 under forcing, in addition to inhibiting summer warming over melting ice (Figure 3d).

322 We compare the SCM results to the Dwyer et al. (2012) analytic solution for the
 323 expected amplitude and phase shift of surface temperature by applying Eq. (6) and (7) to the
 324 1-m and 50-m mixed-layer SCM, where

$$325 \quad Q(t) = \underbrace{[1 - \alpha_i]F_s(t)}_{\text{solar}} - \underbrace{F_0(t)}_{\text{OLR}} + \underbrace{F_B}_{\text{basal heat flux}} + \underbrace{\Delta F_0}_{\text{forcing}}, \quad (8)$$

$$326 \quad \beta = F_T(t). \quad (9)$$

327 Results are similar for the analytic solution (Figure S3a,b, grey lines) and SCM experiments
 328 (Figure S3a,b, black lines), with small differences due to applying discrete monthly solar
 329 forcing and $F_0(t)$ to the SCM. When $F_s(t)$ is instead represented as a cosine function and the
 330 annual-mean value of $F_0(t)$ is used, the amplitude and phase shift of surface temperature in
 331 the SCM exactly matches results from Eq. (6) and (7) (Figure S3c,d). These results from the
 332 mixed-layer SCM and analytic solution demonstrate that the key features of Arctic
 333 seasonality in warming can be produced simply by representing how the effective heat
 334 capacity of the Arctic surface layer evolves with surface temperature.

335 *e. SCM with and without sea-ice thermodynamics*

336 A final way to isolate the role of effective surface heat capacity changes and other
337 thermodynamic processes is to compare SCM experiments with ice to SCM experiments with
338 identical, prescribed albedo changes but no ice. Figure 4a-c shows the same SCM
339 configurations as in Figure 2b-d for select forcing experiments illustrating annually ice-
340 covered, seasonally ice-free, and annually ice-free conditions (solid lines; *Ice* experiments).
341 Overlaid are results for the same SCM configurations, but with a 50-m mixed-layer SCM
342 with no ice and with prescribed surface albedo from the *Ice* experiments (dashed lines; *No*
343 *ice, set albedo* experiments). With identical albedo changes under increased forcing, these *Ice*
344 and *No ice, set albedo* experiments differ only in their inclusion or exclusion of sea-ice
345 thermodynamics.

346 In both the standard SCM (Figure 4a) and the SCM with an annual-mean Planck
347 feedback and constant ice albedo (Figure 4b), ice thermodynamics suppress summer warming
348 over melting ice and enhance winter warming. For surface temperatures below freezing, this
349 enhanced winter warming results from increasing conductive heat flux through thinning ice.
350 When ice thickness is kept constant for the conductive heat flux (Figure 4c), winter warming
351 at temperatures below freezing is instead reduced in the *Ice* experiments compared to the *No*
352 *ice, set albedo* experiments as a result of ice export changes in only the *Ice* experiments. Even
353 with constant ice thickness in the conductive heat flux and reduced winter warming over
354 frozen ice, the transition above freezing temperatures produces enhanced winter warming
355 when ice thermodynamics are included due to a phase delay and amplitude reduction in
356 temperature with increasing effective surface heat capacity. Instead, in the *No ice, set albedo*
357 experiment, the constant effective surface heat capacity for the 50-m mixed layer gives
358 seasonally-constant warming for all forcings. This illustrates the essential role of sea-ice
359 thermodynamics, specifically conductive heat flux changes as frozen ice warms and effective

360 heat capacity changes as frozen ice melts and transitions to open ocean, for the seasonal
361 pattern of Arctic warming.

362 *f. Addition of a lapse-rate feedback to the SCM*

363 Based on analysis of comprehensive GCM experiments, Pithan and Mauritsen (2014)
364 suggest that the winter-peaking lapse-rate feedback is an important driver of seasonality in
365 Arctic warming. To estimate how much additional seasonality in warming the lapse-rate
366 feedback would contribute to the SCM, we add a contribution from this feedback to the
367 surface energy balance, multiplied by the surface warming under forcing compared to $\Delta F_0 =$
368 0. We calculate the lapse-rate feedback for a doubling of CO₂ compared to pre-industrial
369 conditions in CESM slab ocean experiments, described in Section 3, for non-land gridpoints
370 north of 70°N. This gives a fairly constant lapse-rate feedback for gridpoints with below-
371 freezing surface temperatures under CO₂ doubling, and a weaker lapse-rate feedback for
372 gridpoints that exceed the freezing point under CO₂ doubling. Since we add a lapse-rate
373 feedback to the SCM in a forcing experiment ($\Delta F_0 = 12$) that does not warm above the
374 freezing point, we apply the CESM lapse-rate feedback averaged only over gridpoints that
375 remain below freezing under CO₂ doubling ($1 \text{ W m}^{-2} \text{ K}^{-1}$) to the SCM. We show this $\Delta F_0 =$
376 12 forcing experiment in the SCM because it produces warming of similar magnitude to the
377 area-averaged non-land Arctic warming in the CESM CO₂ doubling experiments.

378 Surface temperatures with and without a lapse-rate feedback in the standard SCM are
379 shown in Figure 5 for $\Delta F_0 = 12$ compared to $\Delta F_0 = 0$. In these experiments, the lapse-rate
380 feedback increases winter warming by about 3 degrees, magnifying the early winter warming
381 maximum that exists in the SCM without the lapse-rate feedback. Nevertheless, the majority
382 of seasonality in warming in the SCM is still due to processes other than the lapse-rate
383 feedback. For this forcing, these processes are primarily enhanced warming in winter due to

384 an increase in conductive heat flux through thinning ice, and suppressed warming in summer
385 due to the large effective heat capacity of melting ice.

386 **3. Seasonality of Arctic Warming With and Without Sea Ice in CESM**

387 The above results suggest that in the absence of seasonality in climate feedbacks,
388 seasonality in Arctic warming is fundamentally driven by increasing conductive heat flux
389 through thinning ice and increasing effective heat capacity as ice melts and exposes open
390 ocean. Can we similarly isolate the role of sea ice thermodynamic effects within a GCM?
391 Complementary to previous GCM experiments isolating the impact of sea-ice albedo changes
392 on Arctic warming (Feldl et al., 2017; Graverson et al., 2014), here we use idealized GCM
393 experiments to isolate non-albedo thermodynamic effects of sea ice on Arctic warming.
394 While analogous to SCM experiments in Section 2e, these GCM experiments enable us to
395 include not only the thermodynamic and climate feedback effects incorporated in the SCM,
396 but also more complex polar climate feedbacks and changes in poleward heat transport that
397 the SCM excludes.

398 *a. CESM Experiments*

399 We perform all experiments with the CESM (Hurrell et al., 2013) version 1.2.2, which
400 uses the Community Atmosphere Model version 4 (CAM4; Neale et al., 2013) with a
401 horizontal resolution of $0.9^\circ \times 1.25^\circ$ and 26 vertical levels, the Community Land Model
402 version 4 (CLM4; Oleson et al., 2010) and the Los Alamos Sea Ice Model version 4 (CICE4;
403 Hunke and Lipscomb, 2008). For these experiments, CAM4 is coupled to a slab ocean model
404 (SOM) with a prescribed, spatially heterogeneous monthly climatology of ocean heat flux
405 convergence taken from a fully-coupled pre-industrial control simulation (Bitz et al., 2012).
406 While all CESM SOM experiments have been run with the elevation of Antarctica flattened

407 to 0 m above sea level, this flattening has a negligible impact on Arctic surface temperatures
408 (Hahn et al., 2020), which are the focus here.

409 For all configurations of CESM, CO₂ is abruptly doubled from pre-industrial
410 concentrations before running each simulation for 50 years, with climatologies calculated
411 over the final 30 years, which are near equilibrium. We compare control experiments
412 including full sea-ice thermodynamics (called *Ice*) to experiments with no sea ice, in which
413 ocean temperatures can cool below the freezing point (called *No ice*). As in the SCM, we also
414 run experiments with no sea ice in which we prescribe climatological albedo values over non-
415 land surfaces taken from the *Ice* experiments (called *No ice, set albedo*). In these *No ice, set*
416 *albedo* experiments, the non-land albedo change under CO₂ doubling is by design almost
417 identical to the *Ice* experiments (< 0.7% difference for 70-90°N). Small differences may
418 result from the way we prescribe albedo, using the climatological fraction of incoming visible
419 solar radiation that is reflected at the surface in the *Ice* experiment to prescribe direct and
420 diffuse, visible and near-infrared surface albedos in the *No ice, set albedo* experiment, with
421 zero albedo change by default when there is no sunlight.

422 With nearly identical albedo changes under CO₂ doubling in the *Ice* and *No ice, set*
423 *albedo* experiments, differences between these experiments reflect non-albedo
424 thermodynamic effects of sea ice. All remaining figures are shown for the Arctic from 70-
425 90°N over non-land surfaces.

426 *b. Impact of sea-ice thermodynamics and albedo on Arctic warming*

427 Including sea-ice thermodynamics supports colder winters and warmer summers for
428 *Ice* (Figure 6a) compared to *No ice, set albedo* (Figure 6b) experiments. This is consistent
429 with the small effective heat capacity of ice below freezing compared to open ocean, which
430 gives a larger seasonal amplitude and earlier phasing in near-surface temperature in the *Ice*

431 experiments. As in the fully-coupled CESM2 (Figure 1), the CESM SOM *Ice* experiments
432 simulate a summer minimum and early winter maximum in near-surface warming under CO₂
433 doubling (Figure 6c). In contrast, warming is nearly constant year-round in experiments
434 without sea ice. The main effect of ice albedo changes (*No ice, set albedo* compared to *No*
435 *ice*) is to strengthen warming in the annual mean, with a slightly greater increase in fall
436 warming than the rest of the year. The main impact of sea-ice thermodynamic effects (*Ice*
437 compared to *No ice, set albedo*) is to reduce summer warming, as also seen in SCM
438 experiments. Including thermodynamic effects also slightly increases early winter warming,
439 although winter warming is more comparable for *Ice* compared to *No ice, set albedo*
440 experiments in the GCM than in the SCM.

441 *c. Mechanisms linking sea ice to seasonality in Arctic warming*

442 Figure 6 illustrates that one way in which sea-ice thermodynamics contribute to
443 seasonality in Arctic warming is through suppressing summer warming, consistent with the
444 large effective heat capacity of melting ice. Enhanced early winter warming when including
445 ice thermodynamics in the GCM is also consistent with the effects of increasing conductive
446 heat flux as ice below freezing thins, as seen in the SCM, although additional climate
447 feedbacks also contribute to GCM warming. A slight phase delay in surface temperature as
448 ice melts under CO₂ doubling (Figure 6a) would widen with a transition to a seasonally ice-
449 free Arctic under greater forcing (Figure 1), additionally supporting an early winter warming
450 maximum as a result of effective heat capacity changes. Thus, the role of thermodynamics for
451 seasonality in warming in the GCM appears to align with results in the SCM experiments.

452 In addition to these direct effects of sea-ice thermodynamics, we consider indirect
453 effects of ice thermodynamics on the seasonal pattern of warming via impacts on the lapse-
454 rate feedback. The small effective heat capacity of frozen ice gives surface temperatures a

455 large seasonal amplitude that brings temperatures to the freezing point in summer, where they
456 remain due to the very large effective heat capacity of melting ice. As a result of these
457 relatively warm summer surface temperatures, the pre-industrial *Ice* experiment has weak
458 summer stability (Figure 7a, solid light blue line), compared to strong surface temperature
459 inversions during winter (Figure 7b). In contrast, the annually large effective heat capacity of
460 the ocean surface layer in the pre-industrial *No ice, set albedo* experiment gives surface
461 temperatures a small seasonal amplitude, so that they remain below the freezing point in
462 summer (Figure 7a, dashed light blue line). This produces base-state summer inversions that,
463 combined with the elimination of the latent energy sink of melting ice in this experiment,
464 support stronger surface-trapped warming during summer under doubled CO₂. These results
465 suggest that in addition to suppressing summer warming due to the large effective heat
466 capacity of melting ice, sea-ice thermodynamics may also promote seasonality in warming by
467 inhibiting a positive summertime lapse-rate feedback.

468 To quantify contributions from the lapse-rate and other feedbacks to Arctic warming
469 under CO₂ doubling, we apply the radiative kernel method using CAM3 kernels (Shell et al.,
470 2008; Soden et al., 2008). We also calculate the annual atmospheric heat transport (AHT)
471 convergence as the difference between surface and net TOA fluxes, and additionally subtract
472 atmospheric energy and moisture storage to calculate the seasonal cycle of AHT
473 convergence, following Donohoe et al. (2020a). In addition to changes in AHT under CO₂
474 doubling, we consider changes in the surface energy budget (SEB), which includes both ice
475 export changes and seasonal ocean heat storage in the CESM SOM. Energetic contributions
476 from each feedback ($\lambda_i \Delta T$), the Planck response ($\lambda_p \Delta T$), CO₂ forcing (F), changes in SEB
477 and AHT, and a residual term (ΔR_{res}) are then converted into contributions to near-surface

478 warming (ΔT) for the non-land Arctic based on a local energy budget (Eq. 10), following
 479 previous studies such as Goosse et al. (2018) and Pithan and Mauritsen (2014):

$$480 \quad F + \left(\lambda_p + \sum_i \lambda_i \right) \Delta T + \Delta AHT + \Delta SEB + \Delta R_{res} = 0. \quad (10)$$

481 Annual, summer (June-July-August), and winter (December-January-February) warming
 482 contributions are determined by dividing each term in Eq. (10), all in units of W m^{-2} , by the
 483 magnitude of the non-land Arctic Planck response in the *Ice* experiment ($\lambda_{p,Ice}$) in $\text{Wm}^{-2} \text{K}^{-1}$:

$$484 \quad \Delta T = -\frac{F}{\lambda_{p,Ice}} - \frac{\lambda'_p \Delta T}{\lambda_{p,Ice}} - \frac{\sum_i \lambda_i \Delta T}{\lambda_{p,Ice}} - \frac{\Delta AHT}{\lambda_{p,Ice}} - \frac{\Delta SEB}{\lambda_{p,Ice}} - \frac{\Delta R_{res}}{\lambda_{p,Ice}}, \quad (11)$$

485 where $\lambda'_p = \lambda_p - \lambda_{p,Ice}$ is the difference between the non-land Arctic Planck feedback for a
 486 given experiment, λ_p , and $\lambda_{p,Ice}$.

487 In Figure 8, contributions to non-land Arctic warming in the *Ice* configuration of the
 488 CESM SOM are plotted along the horizontal axis, while contributions to warming in the *No*
 489 *ice, set albedo* configuration are plotted along the vertical axis. The albedo feedback is
 490 identical by design for both experiments. Greater annual-mean warming in the *No ice, set*
 491 *albedo* experiments compared to the *Ice* experiments is mainly contributed by a more-
 492 positive lapse-rate feedback (Figure 8a). This results from a stronger lapse-rate contribution
 493 to summer warming in the *No ice, set albedo* experiments (Figure 8b), while the lapse-rate
 494 contribution to winter warming is similar for both sets of experiments (Figure 8c). In addition
 495 to the lapse-rate feedback, negative ΔSEB due to reduced sea ice export under CO_2 doubling
 496 slightly weakens annual warming in the *Ice* experiment compared to the *No ice, set albedo*
 497 experiment, consistent with the SCM experiments. Seasonally, the ΔSEB contribution
 498 indicates stronger energy transfer from the atmosphere to ocean in summer and from the

499 ocean to atmosphere in winter in the *Ice* experiment, which also contributes to stronger
500 seasonality in warming.

501 The *Ice* and *No ice, set albedo* experiments show similar DJF warming because
502 reduced winter ocean-to-atmosphere heat transfer in the *No ice, set albedo* experiment is
503 compensated by increased winter poleward AHT. Despite reduced seasonal ocean heat
504 storage, the winter lapse-rate feedback remains similarly strong in the *No ice, set albedo*
505 experiment compared to the *Ice* experiment. In contrast to the hypothesis of Dai et al. (2019)
506 and Chung et al. (2021), these results suggest that seasonal heat transfer related to sea-ice
507 insulation loss is not necessary for a strong wintertime lapse-rate feedback.

508 A caveat to this feedback analysis in the *No ice, set albedo* experiments is that we use
509 radiative kernels derived from experiments that include sea ice. In reality, we would expect
510 that a colder and drier lower troposphere during summer in the *No ice, set albedo*
511 experiments (Figure 7) would diminish the effect of atmospheric temperature changes on
512 TOA radiation (the temperature radiative kernel), and thus lead to a weaker summer lapse-
513 rate feedback than that shown in Figure 8. We test the sensitivity of feedback warming
514 contributions to this choice of radiative kernel by substituting kernels from other months and
515 find similar results, with the lapse-rate feedback still contributing most to greater summer
516 warming in the *No ice, set albedo* experiment compared to the *Ice* experiment (see
517 Supplementary Text S1).

518 **4. Summary and Conclusions**

519 We use idealized experiments with certain sea ice processes individually inactivated
520 in a GCM as well as a simpler model in order to disentangle potential causes of seasonality in
521 Arctic warming under CO₂ forcing. A simple SCM is able to capture key features of Arctic
522 warming seasonality: a summer minimum and early winter maximum in Arctic warming,

523 shifting to a late winter maximum under greater forcing. Several factors contribute to the
524 warming seasonality in this model, including seasonality in the Planck response, albedo
525 feedback, and conductive heat flux through ice. In the absence of seasonality in climate
526 feedbacks, the SCM simulates peak early winter warming over ice below freezing due to
527 increasing conductive heat flux as ice thins, while the large effective heat capacity of melting
528 ice suppresses summer warming. When conductive heat flux variations with ice thickness are
529 further eliminated, the SCM still exhibits peak early winter warming due to a phase delay and
530 amplitude reduction in surface temperature as perennial sea ice transitions to a seasonally ice-
531 free ocean. While frozen sea ice warms quickly to the melting point in summer and cools
532 quickly to very cold winter temperatures in the zero-forcing experiment, exposed open ocean
533 in fall and early winter at increased forcing undergoes slower seasonal warming and cooling
534 due to its larger effective heat capacity, keeping temperatures above freezing later in the year
535 and supporting peak early winter warming relative to the zero-forcing experiment. With
536 greater forcing, this transition and associated amplitude reduction from colder ice to warmer
537 ocean temperatures occurs later in the year, producing peak warming in late winter. SCM
538 experiments demonstrate that representing the evolving effective heat capacity of the Arctic
539 surface layer is alone sufficient to reproduce the key features of seasonality in Arctic
540 warming.

541 Consistent with the SCM results, GCM experiments with doubled CO₂ simulate peak
542 early winter warming and weak summer warming when sea ice is included. Comparison of
543 experiments with sea ice to those with identical, prescribed surface albedo changes but no sea
544 ice under CO₂ forcing suggests that seasonality in Arctic warming depends on sea-ice
545 thermodynamic effects in both the SCM and GCM. Sea ice melt suppresses summer warming
546 while winter warming is amplified by increasing conductive heat flux through thinning ice

547 and increasing effective heat capacity as ice melts and exposes open ocean. In the GCM, sea
548 ice also damps summer warming by inhibiting a positive summer lapse-rate feedback due to
549 weak base-state atmospheric stability (as a result of the small effective heat capacity of frozen
550 sea ice in non-summer months, which gives surface temperatures a large seasonal amplitude
551 and produces relatively warm summer surface temperatures) and minimal near-surface
552 warming in the presence of summer sea-ice melt. In winter, weaker seasonal ocean heat
553 release to the atmosphere in the *No ice, set albedo* GCM experiments is compensated by an
554 increase in poleward AHT. This supports similar winter warming for the *No ice, set albedo*
555 and the *Ice* experiments in the GCM, as does a strong winter lapse-rate feedback with only
556 the albedo effects of sea-ice loss.

557 Similar to previous studies, our results support a key role of sea ice in setting the
558 seasonality of Arctic warming. Here we highlight effective heat capacity changes as a
559 fundamental mechanism for this seasonality in warming, with results demonstrating the
560 utility of simpler models for understanding mechanisms of Arctic warming. Idealized GCM
561 experiments also offer insight into the interconnected effects of sea ice on surface albedo
562 changes, seasonal ocean heat storage, and insulation loss and their impacts on the lapse-rate
563 feedback. These experiments suggest that a strong wintertime lapse-rate feedback can be
564 produced with the albedo effects of sea-ice loss alone, in contrast to the idea that seasonal
565 heat transfer related to sea-ice insulation loss is necessary to kickstart the winter lapse-rate
566 feedback.

567 Disentangling these effects of sea ice is difficult in GCMs in part because diagnostic
568 frameworks like warming contribution analyses implicitly include interactions between
569 different contributors. Feedbacks like the lapse-rate feedback are also impacted by heat
570 capacity effects on surface warming, which are not explicitly quantified in this warming

571 contribution framework. This limitation highlights a need for alternative frameworks, simpler
572 models, and idealized experiments to isolate the mechanisms of polar amplification and
573 interactions between mechanisms, as also suggested by Boeke et al. (2021) and Feldl et al.
574 (2020). The key role of effective heat capacity changes for seasonality in Arctic warming,
575 emphasized here with a simple model and idealized GCM experiments, also highlights a need
576 to accurately model the transition from perennial ice to seasonally ice-free conditions in
577 comprehensive GCMs in order to project the timing and magnitude of peak Arctic warming.

578 *Acknowledgments*

579 We acknowledge high-performance computing support from Cheyenne
580 ([doi:10.5065/D6RX99HX](https://doi.org/10.5065/D6RX99HX)) provided by NCAR's Computational and Information Systems
581 Laboratory (2019), sponsored by the National Science Foundation. LCH was supported by
582 the National Science Foundation (NSF) Graduate Research Fellowship Grant DGE-1762114
583 and the ARCS Foundation Fellowship. KCA was supported by National Science Foundation
584 Grants AGS-1752796 and OCE-1850900 and an Alfred P. Sloan Research Fellowship. IE
585 was supported by NSF OPP-1643445. CMB was supported by NSF OPP-1643431.

586 *Data Availability Statement*

587 The Eisenman and Wettlaufer (2009) single-column sea ice model is available from
588 <https://eisenman-group.github.io> (sea_ice_model_EW09.m). The CESM2 *IpctCO2-4xext*
589 experiments can be found in the Earth System Grid Federation (ESGF) repository at
590 <https://esgf-node.llnl.gov/projects/esgf-llnl/>. Monthly climatologies of model output from
591 idealized CESM experiments are available at <https://doi.org/10.5281/zenodo.4925048>.

592

593

594

REFERENCES

- 595 Bintanja, R., Graverson, R. & Hazeleger, W. (2011). Arctic winter warming amplified by the
596 thermal inversion and consequent low infrared cooling to space. *Nature Geosci* 4, 758–
597 761. <https://doi.org/10.1038/ngeo1285>
- 598 Bintanja, R., & van der Linden, E. (2013). The changing seasonal climate in the
599 Arctic. *Scientific Reports* 3, 1556. <https://doi.org/10.1038/srep01556>
- 600 Bitz, C.M., Shell, K.M., Gent, P.R., Bailey, D.A., Danabasoglu, G., Armour, K.C., Holland,
601 M.M., & Kiehl, J.T. (2012). Climate Sensitivity of the Community Climate System
602 Model, Version 4. *Journal of Climate*, 25, 3053–3070. [https://doi.org/10.1175/JCLI-D-](https://doi.org/10.1175/JCLI-D-11-00290.1)
603 [11-00290.1](https://doi.org/10.1175/JCLI-D-11-00290.1)
- 604 Boeke, R. C., Taylor, P. C., & Sejas, S. A. (2021). On the nature of the Arctic's positive
605 lapse-rate feedback. *Geophys. Res. Lett.* 48,
606 e2020GL091109. <https://doi.org/10.1029/2020GL091109>
- 607 Chung, E.-S., Ha, K.-J., Timmermann, A., Stuecker, M. F., Bodai, T., & Lee, S.-
608 K. (2021). Cold-season Arctic amplification driven by Arctic ocean-mediated seasonal
609 energy transfer. *Earth's Future* 9,
610 e2020EF001898. <https://doi.org/10.1029/2020EF001898>
- 611 Computational and Information Systems Laboratory. 2019. Cheyenne: HPE/SGI ICE XA
612 System (University Community Computing). Boulder, CO: National Center for
613 Atmospheric Research. <https://doi.org/10.5065/D6RX99HX>
- 614 Cronin, T. W., & Jansen, M. F. (2015). Analytic radiative-advective equilibrium as a model
615 for high-latitude climate. *Geophys. Res. Lett.* 43, 449–457.
616 <https://doi.org/10.1002/2015GL067172>

617 Dai, A., Luo, D., Song, M., & Liu, J. (2019). Arctic amplification is caused by sea-ice loss
618 under increasing CO₂. *Nat. Commun.* 10, 121. [https://doi.org/10.1038/s41467-018-07954-](https://doi.org/10.1038/s41467-018-07954-9)
619 [9](https://doi.org/10.1038/s41467-018-07954-9)

620 Danabasoglu, G., Lamarque, J.-F., Bacmeister, J., Bailey, D. A., DuVivier, A. K., Edwards,
621 J., et al. (2020). The Community Earth System Model Version 2 (CESM2). *Journal of*
622 *Advances in Modeling Earth Systems*, 12,
623 e2019MS001916. <https://doi.org/10.1029/2019MS001916>

624 Deser, C., Tomas, R., Alexander, M., & Lawrence, D. (2010). The Seasonal Atmospheric
625 Response to Projected Arctic Sea Ice Loss in the Late Twenty-First Century. *J.*
626 *Clim.* 23(2), 333-351. <https://doi.org/10.1175/2009JCLI3053.1>

627 Donohoe, A., Armour, K. C., Roe, G. H., Battisti, D. S., & Hahn, L. (2020a). The partitioning
628 of meridional heat transport from the Last Glacial Maximum to CO₂ quadrupling in
629 coupled climate models. *J. Clim.* 33(10), 4141-4165. [https://doi.org/10.1175/JCLI-D-19-](https://doi.org/10.1175/JCLI-D-19-0797.1)
630 [0797.1](https://doi.org/10.1175/JCLI-D-19-0797.1)

631 Dwyer, J. G., Biasutti, M., Sobel, & A. H. (2012). Projected changes in the seasonal cycle of
632 surface temperature. *J. Clim.* 25(18), 6359-6374. [https://doi.org/10.1175/JCLI-D-11-](https://doi.org/10.1175/JCLI-D-11-00741.1)
633 [00741.1](https://doi.org/10.1175/JCLI-D-11-00741.1)

634 Eisenman, I., & Wettlaufer, J. S. (2009). Nonlinear threshold behavior during the loss of
635 Arctic sea ice. *PNAS* 106 (1), 28-32. <https://doi.org/10.1073/pnas.0806887106>

636 Feldl, N., Bordoni, S., & Merlis, T. M. (2017). Coupled high-latitude climate feedbacks and
637 their impact on atmospheric heat transport. *J. Clim.* 30, 189–201.
638 <https://doi.org/10.1175/JCLI-D-16-0324.1>

639 Feldl, N., Po-Chedley, S., Singh, H.K.A. *et al.* (2020). Sea ice and atmospheric circulation
640 shape the high-latitude lapse rate feedback. *npj Clim Atmos Sci* 3, 41.
641 <https://doi.org/10.1038/s41612-020-00146-7>

642 Goosse, H., Kay, J. E., Armour, K. C., Bodas-Salcedo, A., Chepfer, H., Docquier, D., et
643 al. (2018). Quantifying climate feedbacks in polar regions. *Nat. Commun.*
644 9, 1919. <https://doi.org/10.1038/s41467-018-04173-0>

645 Graversen, R. G., Langen, P. L., & Mauritsen, T. (2014). Polar amplification in CCSM4:
646 Contributions from the lapse rate and surface albedo feedbacks. *J.Clim.* 27, 4433–4450.
647 <https://doi.org/10.1175/JCLI-D-13-00551.1>

648 Hahn, L. C., Armour, K. C., Battisti, D. S., Donohoe, A., Pauling, A. G., & Bitz, C.
649 M. (2020). Antarctic elevation drives hemispheric asymmetry in polar lapse rate
650 climatology and feedback. *Geophys. Res. Lett.* 47,
651 e2020GL088965. <https://doi.org/10.1029/2020GL088965>

652 Hahn, L. C., Armour, K. C., Zelinka, M. D., Bitz, C. M., & Donohoe, A. (2021).
653 Contributions to Polar Amplification in CMIP5 and CMIP6 Models. *Frontiers in Earth*
654 *Science*, in press.

655 Holland, M. M., & Bitz, C. M. (2003). Polar amplification of climate change in coupled
656 models. *Clim. Dyn.* 21, 221–232. <https://doi.org/10.1007/s00382-003-0332-6>

657 Hunke, E., & Lipscomb, W. (2008). CICE: The Los Alamos sea ice model, documentation
658 and software, version 4.0 (Tech. Rep. LA-CC-06-012). Los Alamos, NM: Los Alamos
659 National Laboratory.

660 Hurrell, J. W., Holland, M. M., Gent, P. R., Ghan, S., Kay, J. E., Kushner, P. J., et al.
661 (2013). The Community Earth System Model: A framework for collaborative

662 research. *Bull. Am. Meteor. Soc.* 94(9), 1339–1360. <https://doi.org/10.1175/BAMS-D-12->
663 [00121.1](https://doi.org/10.1175/BAMS-D-12-00121.1)

664 Kalnay E, *et al.* (1996). The NCEP/NCAR 40-year reanalysis project. *Bull. Am. Meteor. Soc.*
665 77, 437–471. [https://doi.org/10.1175/1520-](https://doi.org/10.1175/1520-0477(1996)077%3C0437:TNYRP%3E2.0.CO;2)
666 [0477\(1996\)077%3C0437:TNYRP%3E2.0.CO;2](https://doi.org/10.1175/1520-0477(1996)077%3C0437:TNYRP%3E2.0.CO;2)

667 Lu, J., & Cai, M. (2009). Seasonality of polar surface warming amplification in climate
668 simulations. *Geophys. Res. Lett.* 36, L16704, <https://doi.org/10.1029/2009GL040133>

669 Manabe, S., & Stouffer, R. J. (1980). Sensitivity of a global climate model to an increase of
670 CO₂ concentration in the atmosphere. *J. Geophys. Res.* 85(C10), 5529-5554.
671 <https://doi.org/10.1029/JC085iC10p05529>

672 Mann, M. E., & Park, J. (1996). Greenhouse warming and changes in the seasonal cycle of
673 temperature: Model versus observations. *Geophys. Res. Lett.* 23, 1111–1114.
674 <https://doi.org/10.1029/96GL01066>

675 Maykut, G. A., & Untersteiner, N. (1971). Some results from a time-dependent
676 thermodynamic model of sea ice. *J. Geophys. Res.* 76, 1550–1575.
677 <https://doi.org/10.1029/JC076i006p01550>

678 Maykut, G. A., & Church, P. E. (1973). Radiation climate of Barrow, Alaska, 1962–66. *J.*
679 *Appl. Meteor.* 12, 620–628. [https://doi.org/10.1175/1520-](https://doi.org/10.1175/1520-0450(1973)012%3C0620:RCOBA%3E2.0.CO;2)
680 [0450\(1973\)012%3C0620:RCOBA%3E2.0.CO;2](https://doi.org/10.1175/1520-0450(1973)012%3C0620:RCOBA%3E2.0.CO;2)

681 Nakamura, N., & Oort A. H. (1988). Atmospheric heat budgets of the polar-regions. *J.*
682 *Geophys. Res.* 93, 9510–9524. <https://doi.org/10.1029/JD093iD08p09510>

683 Neale, R. B., Richter, J., Park, S., Lauritzen, P. H., Vavrus, S. J., Rasch, P. J., & Zhang, M.
684 (2013). The mean climate of the Community Atmosphere Model (CAM4) in forced SST

685 and fully coupled experiments. *Journal of Climate*, 26, 5150–5168.
686 <https://doi.org/10.1175/JCLI-D-12-00236.1>

687 Oleson, K., Lawrence, D., Bonan, G., Flanner, M., Kluzek, E., Lawrence, P., et al. (2010).
688 Technical description of version 4.0 of the Community Land Model (CLM) (Tech. Rep.
689 TN-478+STR). Boulder, CO: National Center for Atmospheric Research.

690 Payne, A. E., Jansen, M. F., & Cronin, T. W. (2015). Conceptual model analysis of the
691 influence of temperature feedbacks on polar amplification. *Geophys. Res. Lett.* 42, 9561–
692 9570. <https://doi.org/10.1002/2015GL065889>

693 Pithan, F., & Mauritsen, T. (2014). Arctic amplification dominated by temperature feedbacks
694 in contemporary climate models. *Nat. Geosci.* 7, 181–184.
695 <https://doi.org/10.1038/ngeo2071>

696 Pithan, F., Medeiros, B., & Mauritsen, T. (2014). Mixed-phase clouds cause climate model
697 biases in Arctic wintertime temperature inversions. *Clim. Dyn.* 43, 289–303.
698 <https://doi.org/10.1007/s00382-013-1964-9>

699 Screen, J. A., & Simmonds, I. (2010a). The central role of diminishing sea ice in recent
700 Arctic temperature amplification. *Nature* 464, 1334–1337.
701 <https://doi.org/10.1038/nature09051>

702 Screen, J. A., & Simmonds, I. (2010b). Increasing fall-winter energy loss from the Arctic
703 Ocean and its role in Arctic temperature amplification. *Geophys. Res. Lett.* 37, L16707.
704 <https://doi.org/10.1029/2010GL044136>

705 Sejas, S. A., Cai, M., Hu, A., Meehl, G. A., Washington, W., & Taylor, P. C. (2014).
706 Individual Feedback Contributions to the Seasonality of Surface Warming. *J.*
707 *Clim.* 27(14), 5653–5669. <https://doi.org/10.1175/JCLI-D-13-00658.1>

708 Serreze, M. C., Barrett, A. P., Stroeve, J. C., Kindig, D. N., & Holland, M. M. (2009). The
709 emergence of surface-based Arctic amplification. *The Cryosphere* 3, 11–19.
710 <https://doi.org/10.5194/tc-3-11-2009>

711 Shell, K. M., Kiehl, J. T., & Shields, C. A. (2008). Using the radiative kernel technique to
712 calculate climate feedbacks in NCAR’s Community Atmospheric Model. *Journal of*
713 *Climate*, 21, 2269–2282. <https://doi.org/10.1175/2007JCLI2044.1>

714 Soden, B. J., Held, I. M., Colman, R., Shell, K. M., Kiehl, J. T., & Shield, C.
715 A. (2008). Quantifying climate feedbacks using radiative kernels. *Journal of*
716 *Climate*, 21, 3504–3520. <https://doi.org/10.1175/2007JCLI2110.1>

717 Taylor, K. E., Crucifix, M., Braconnot, P., Hewitt, C. D., Doutriaux, C., Broccoli, A. J.,
718 & Webb, M. J. (2007). Estimating shortwave radiative forcing and response in climate
719 models. *J. Clim.* 20(11), 2530–2543. <https://doi.org/10.1175/JCLI4143.1>

720 Wagner, T. J. W., & Eisenman, I. (2015). False alarms: How early warning signals falsely
721 predict abrupt sea ice loss. *Geophys. Res. Lett.* 42, 10,333–10,341.
722 <https://doi.org/10.1002/2015GL066297>

723 Yoshimori, M., Abe-Ouchi, A., Watanabe, M., Oka, A., & Ogura, T. (2014). Robust
724 Seasonality of Arctic Warming Processes in Two Different Versions of the MIROC
725 GCM. *J. Clim.* 27(16), 6358-6375. <https://doi.org/10.1175/JCLI-D-14-00086.1>

726

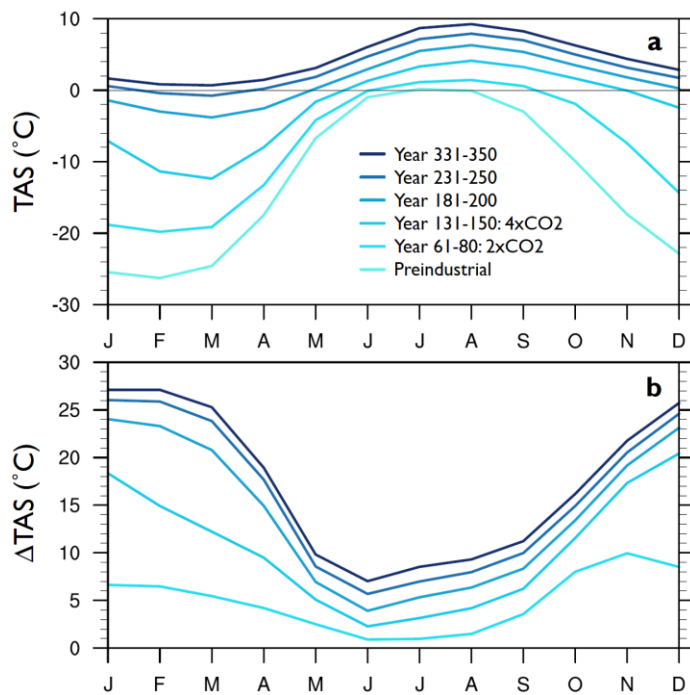
727

728

729

730

FIGURES



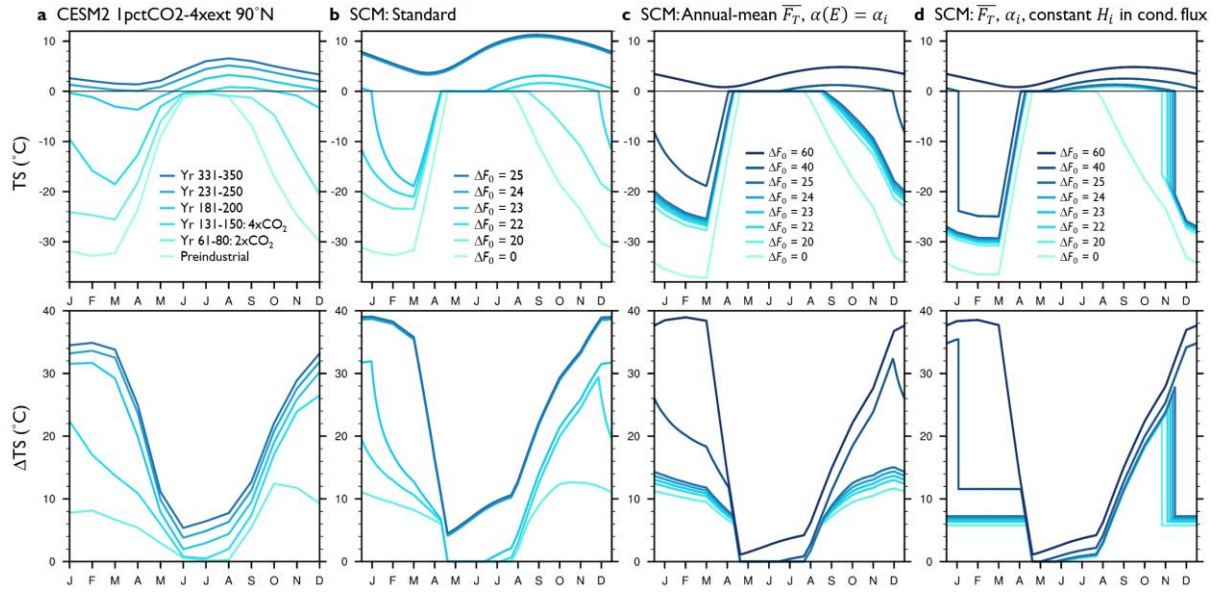
731

732 Figure 1. (a) Near-surface air temperature (TAS; °C) over non-land surfaces from 70-90°N in
 733 a 350-year-long 1% yr⁻¹ CO₂ ramping experiment (*1pctCO2-4xext*) in CESM2 and a 150-
 734 year-long pre-industrial control (*piControl*) experiment from which it was initialized;
 735 averages are taken over years 1-150 of the *piControl* experiment and over selected 20-year
 736 periods of the *1pctCO2-4xext* experiment, with years 61-80 centered on the time of CO₂
 737 doubling and years 131-150 centered on the time of CO₂ quadrupling. (b) TAS anomalies for
 738 each period in the *1pctCO2-4xext* experiment calculated relative to the *piControl* experiment.

739

740

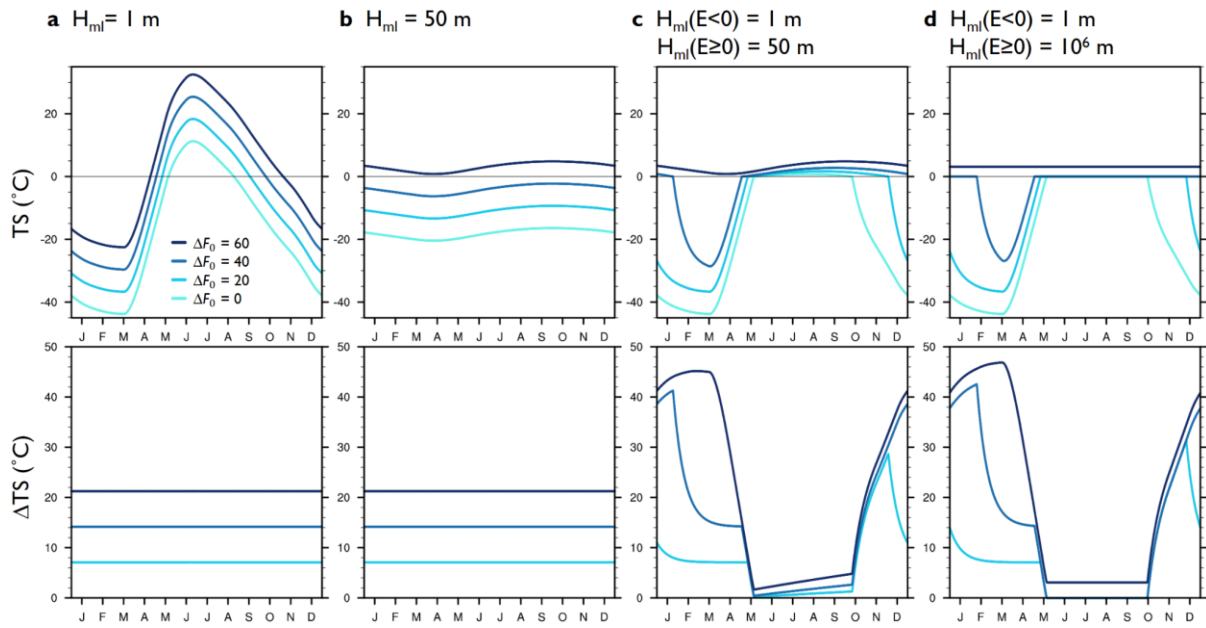
741



742

743 Figure 2. (a) Surface temperature (TS; °C) for the *1pctCO2-4xext* and *piControl* experiments
 744 at 90°N in CESM2, and for surface forcing experiments in (b) the standard SCM, (c) the
 745 SCM with annual-mean $F_T(t)$ and constant $\alpha(E) = \alpha_i$, and (d) the SCM with annual-mean
 746 $F_T(t)$, constant $\alpha(E) = \alpha_i$, and constant ice thickness H_i when calculating the conductive
 747 heat flux through frozen ice, which is set to the annual-mean H_i from the $\Delta F_0 = 0$ experiment
 748 with annual-mean $F_T(t)$ and constant $\alpha(E) = \alpha_i$. The bottom row shows TS anomalies
 749 compared to pre-industrial CO₂ (for CESM2) or $\Delta F_0 = 0$ (for the SCM).

750



751

752 Figure 3. Surface temperature (TS; °C) for various surface forcings and mixed-layer depths in

753 the SCM run as a mixed layer with annual-mean $F_T(t)$ and constant $\alpha(E) = \alpha_i$. TS

754 anomalies for each forcing experiment compared to $\Delta F_0 = 0$ are shown in the bottom row.

755

756

757

758

759

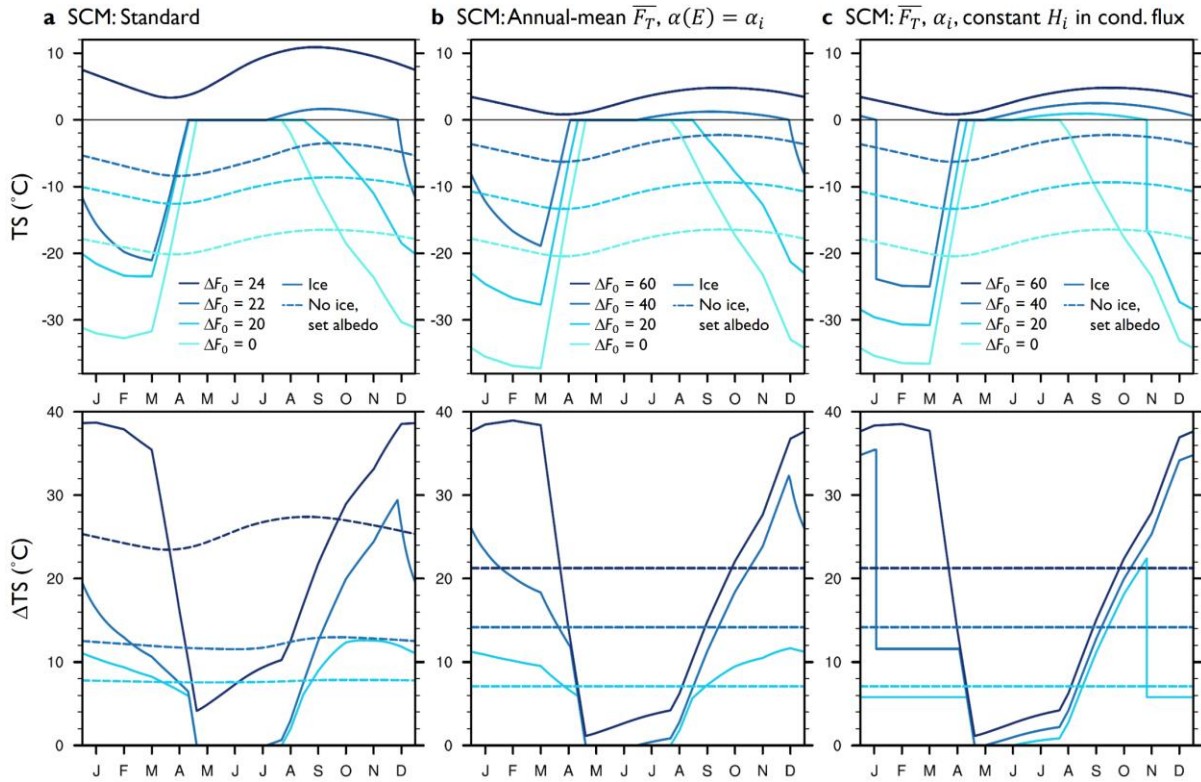
760

761

762

763

764

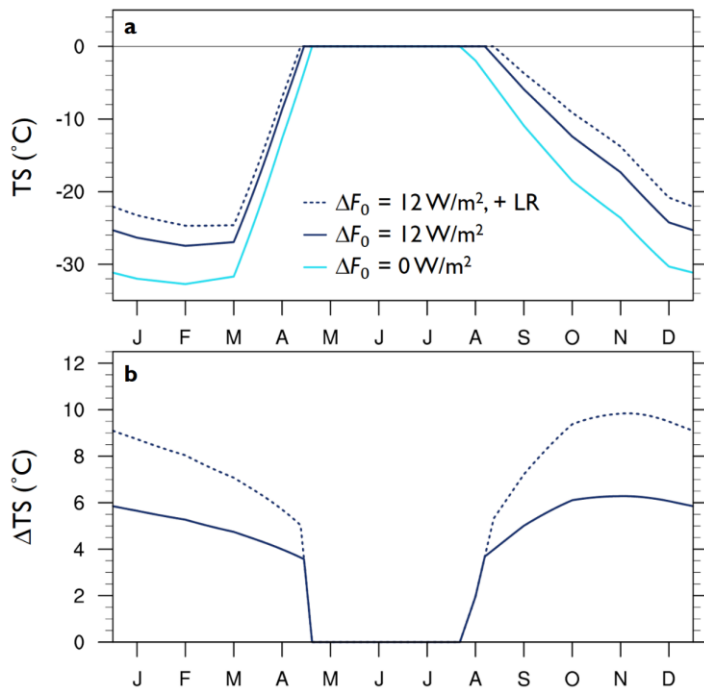


765

766 Figure 4. As in Figure 2b-d for select surface forcing experiments, solid lines show surface
 767 temperature (TS; °C) in (a) the standard SCM, (b) the SCM with annual-mean $F_T(t)$ and
 768 constant $\alpha(E) = \alpha_i$, and (c) the SCM with annual-mean $F_T(t)$, constant $\alpha(E) = \alpha_i$, and
 769 constant ice thickness H_i when calculating the conductive heat flux through frozen ice, which
 770 is set to the annual-mean H_i from the $\Delta F_0 = 0$ experiment with annual-mean $F_T(t)$ and
 771 constant $\alpha(E) = \alpha_i$. Dashed lines show TS for identical experiments, but with a mixed-layer
 772 SCM and prescribed surface albedo from the experiments with ice. The bottom row shows
 773 TS anomalies compared to the $\Delta F_0 = 0$ experiment.

774

775



776

777 Figure 5. (a) Surface temperature (TS; °C) and (b) anomalies in TS for $\Delta F_0 = 12$ compared to

778 $\Delta F_0 = 0$ in the standard SCM (solid lines) and the standard SCM with a simple lapse-rate

779 feedback added (dashed line).

780

781

782

783

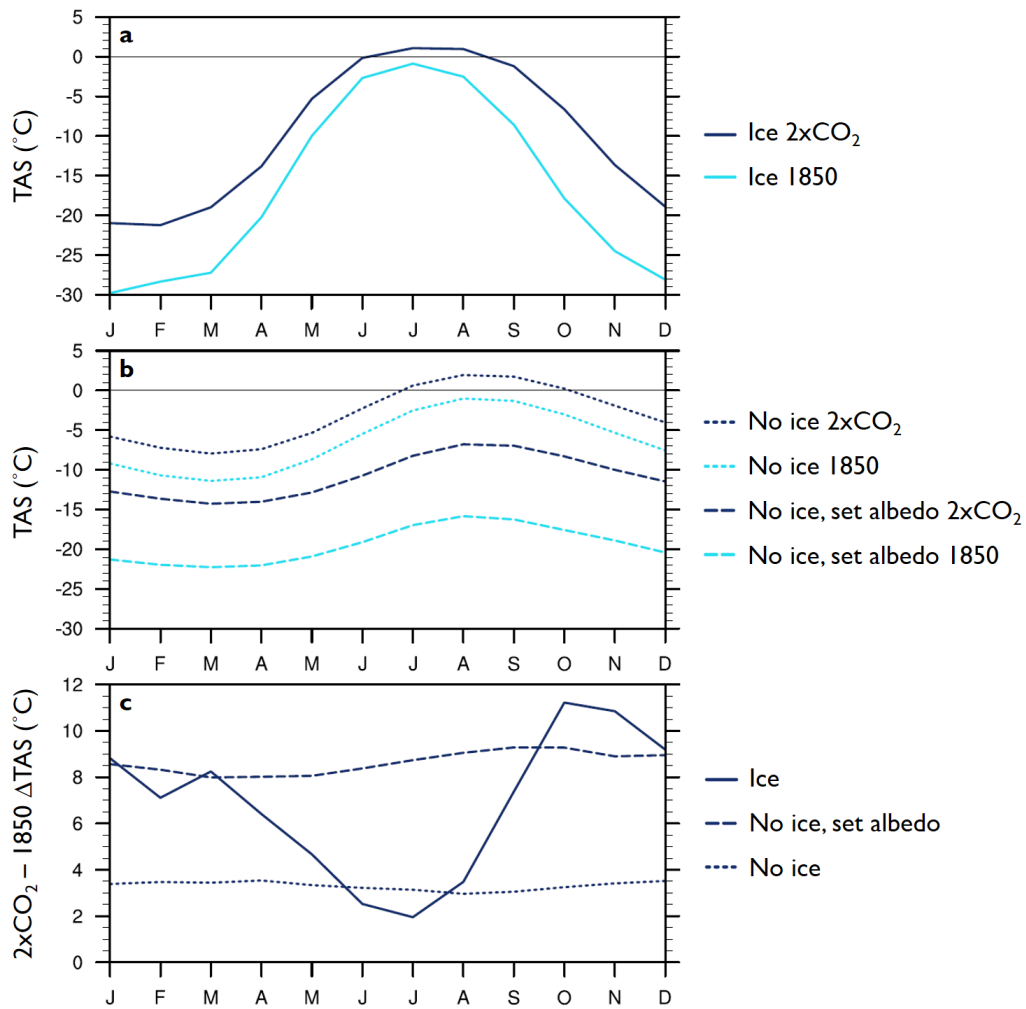
784

785

786

787

788



789

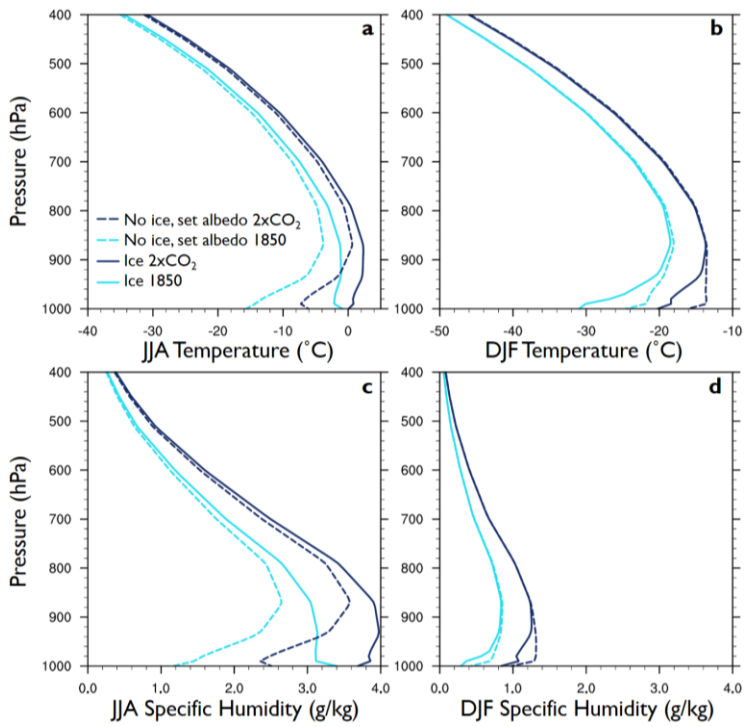
790 Figure 6. Near-surface temperature (TAS; °C) over non-land surfaces from 70-90°N for the
 791 CESM SOM (a) *Ice* experiment and (b) *No ice* and *No ice, set albedo* experiments under pre-
 792 industrial (light blue) and doubled CO₂ (dark blue). (c) TAS anomalies for doubled CO₂
 793 compared to pre-industrial experiments (e.g. *Ice* = *Ice 2xCO₂* minus *Ice 1850*; *No ice* = *No*
 794 *ice 2xCO₂* minus *No ice 1850*).

795

796

797

798



799

800 Figure 7. (a,b) Atmospheric temperature ($^{\circ}\text{C}$) and (c,d) specific humidity (g/kg) over non-
 801 land surfaces from $70\text{-}90^{\circ}\text{N}$ for June-July-August (JJA; a,c) and December-January-February
 802 (DJF; b,d) in the *Ice* (solid) and *No ice, set albedo* (dashed) CESM SOM experiments under
 803 pre-industrial conditions (light blue) and doubled CO_2 (dark blue).

804

805

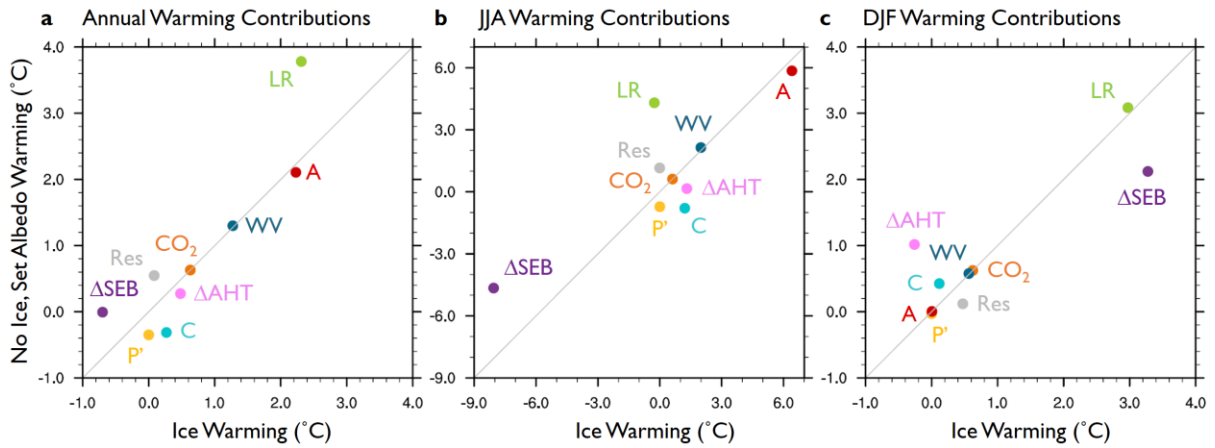
806

807

808

809

810



811

812 Figure 8. Contributions to (a) annual-mean, (b) JJA, and (c) DJF warming (°C) over non-land

813 surfaces from 70-90°N under CO₂ doubling in the CESM SOM in the *Ice* configuration

814 (horizontal axis) and *No ice, set albedo* configuration (vertical axis). Warming contributions

815 are shown for the lapse-rate (LR), surface albedo (A), water-vapor (WV), and cloud (C)

816 feedbacks, the variation in the Planck response from its value in the *Ice* experiment (P'), CO₂

817 forcing (CO₂), change atmospheric heat transport convergence (ΔAHT) and surface energy

818 budget (ΔSEB), which includes ice export and seasonal ocean heat storage, and residual term

819 (Res).

820

821

822

823

824

825

826

827

829 **Text S1.** Kernel sensitivity test for the *No ice, set albedo* experiments

830

831

832

833

834

835

836

837

838

839

840

841

842

843

844

845

846

847

848

849

850

851

852

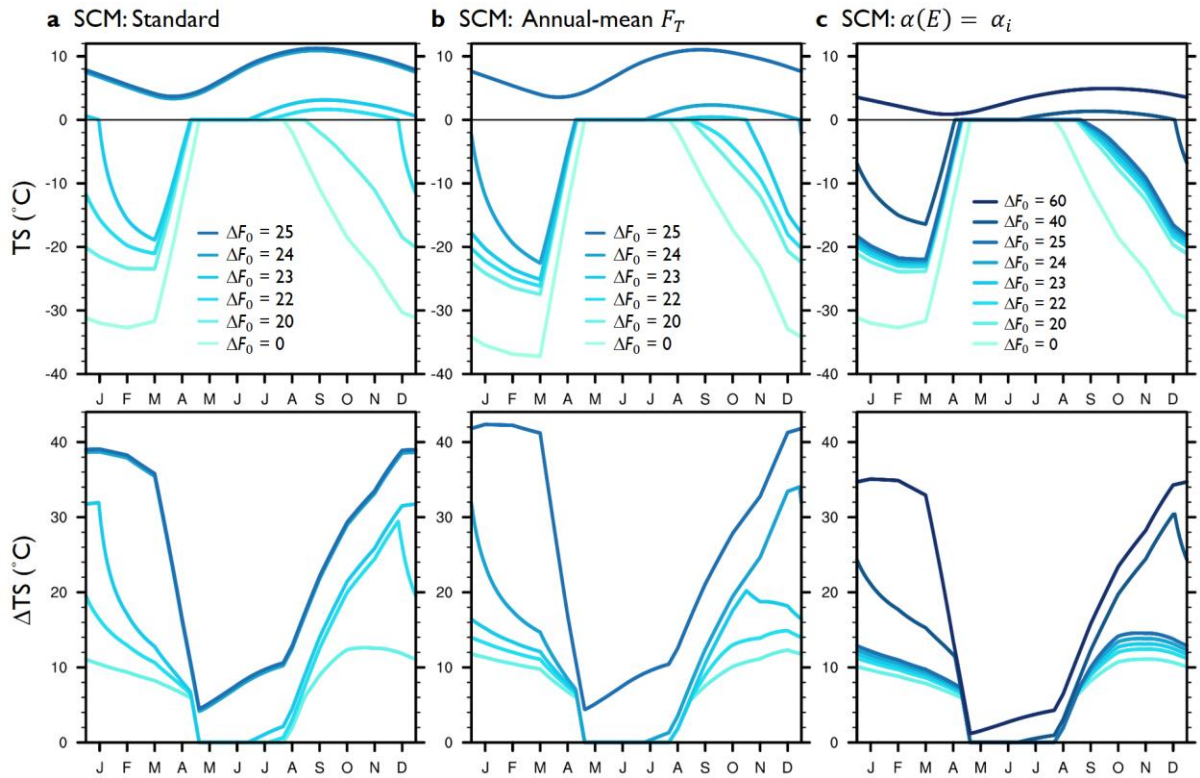
853

854

855

856

857

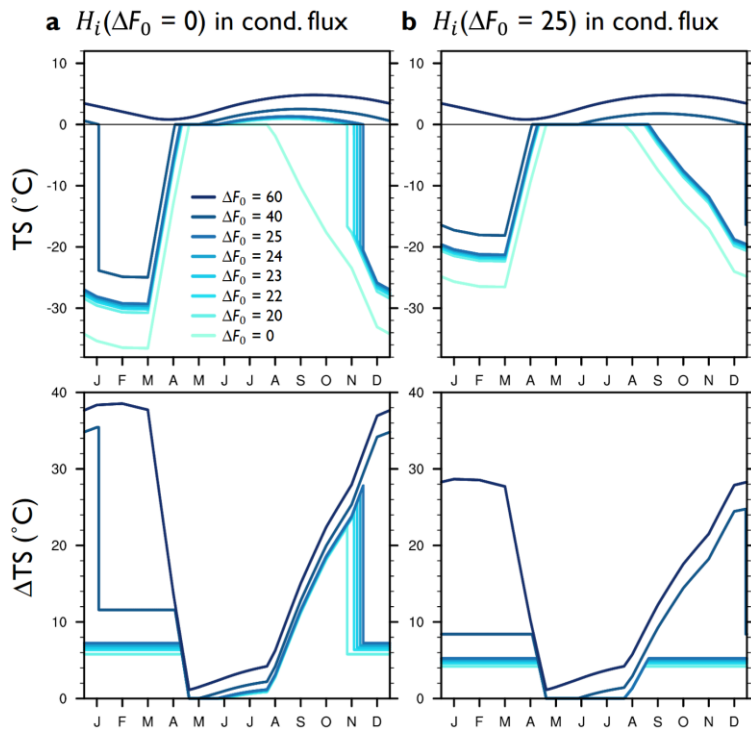


858

859 **Figure S1.** Surface temperature (TS; °C) for surface forcing experiments in (a) the standard
 860 SCM, (b) the SCM with annual-mean $F_T(t)$, and (c) the SCM with constant $\alpha(E) = \alpha_i$. The
 861 bottom row shows TS anomalies compared to the $\Delta F_0 = 0$ experiment.

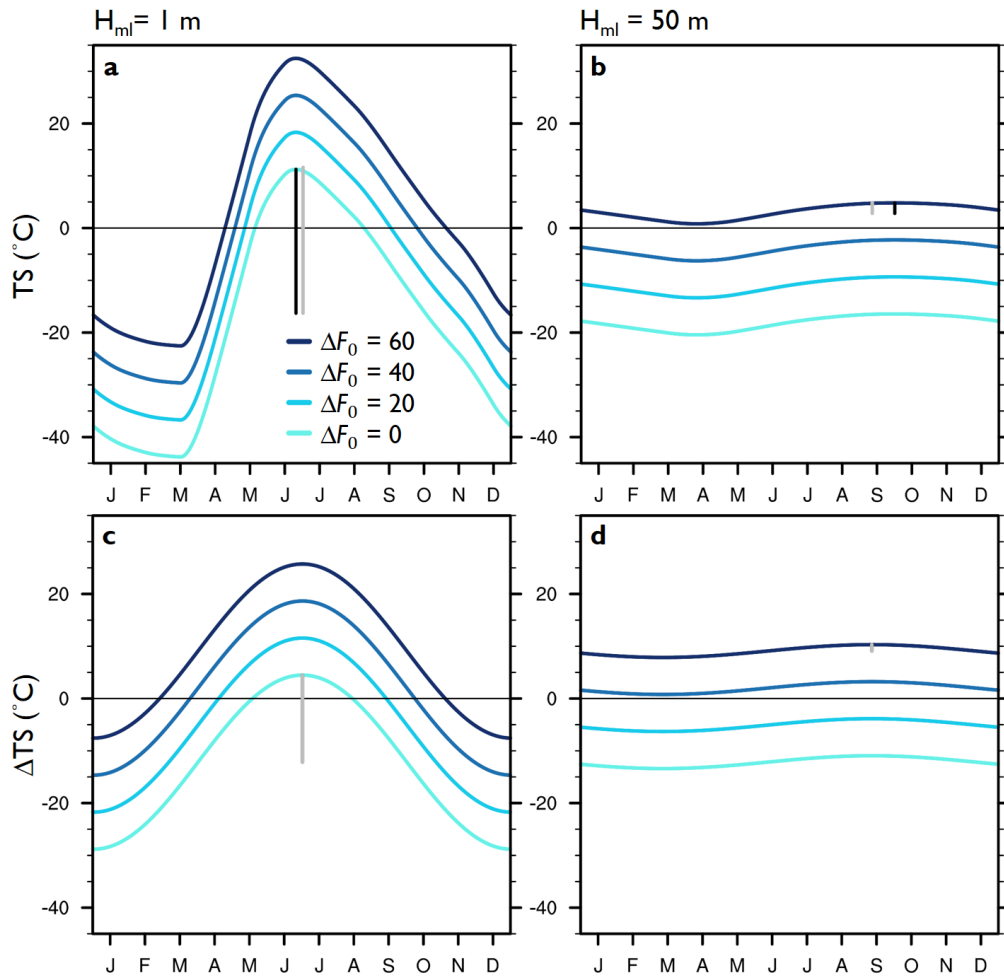
862

863



864

865 **Figure S2.** As in Figure 2d, surface temperature (TS; °C) for surface forcing experiments in
 866 the SCM with annual-mean $F_T(t)$, constant $\alpha(E) = \alpha_i$, and constant ice thickness H_i when
 867 calculating the conductive heat flux through frozen ice, which is set to the annual-mean H_i
 868 from (a) the $\Delta F_0 = 0$ experiment ($H_i = 3.2$ m) and (b) the $\Delta F_0 = 25$ experiment ($H_i = 1.0$ m)
 869 with annual-mean $F_T(t)$ and constant $\alpha(E) = \alpha_i$. The bottom row shows TS anomalies
 870 compared to the $\Delta F_0 = 0$ experiment.



871

872 **Figure S3.** As in Figure 3a,b top, for (a,b) the mixed-layer SCM with annual-mean $F_T(t)$ and
 873 constant $\alpha(E) = \alpha_i$, and (c,d) the same model, but with sinusoidal solar forcing $F_s(t)$ and
 874 annual-mean $F_0(t)$. The black vertical lines indicate the timing and amplitude of maximum
 875 surface temperature for the SCM, while the grey lines show the analytical solution.

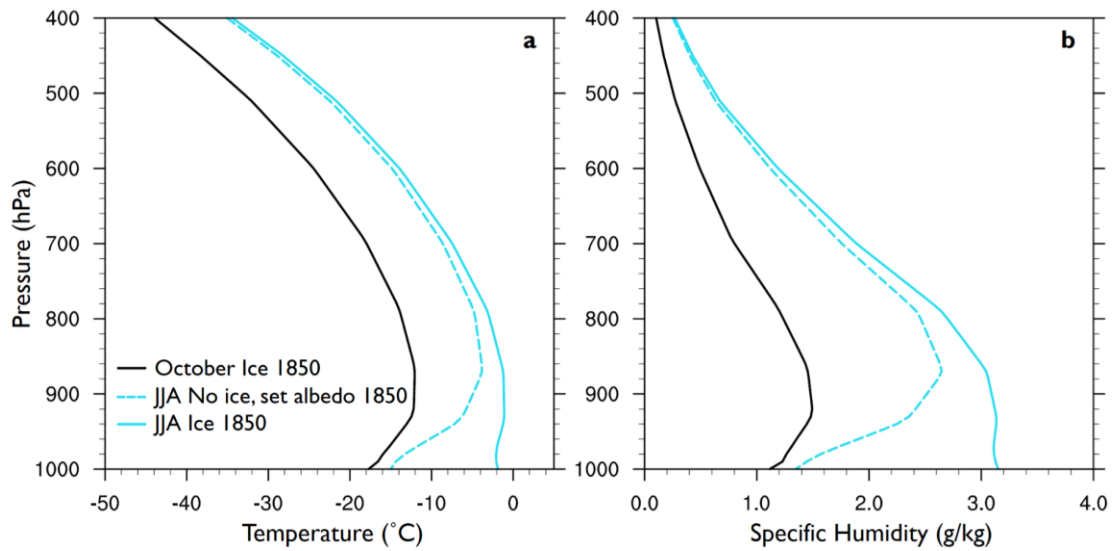
876

877

878

879

880



881

882 **Figure S4.** (a) Atmospheric temperature ($^{\circ}\text{C}$) and (b) specific humidity (g/kg) over non-land
 883 surfaces from $70\text{-}90^{\circ}\text{N}$ under pre-industrial forcing in the *No ice, set albedo* experiment
 884 during June-July-August (JJA; dashed light blue) and in the *Ice* experiment during JJA (solid
 885 light blue) and October (black).

886

887

888

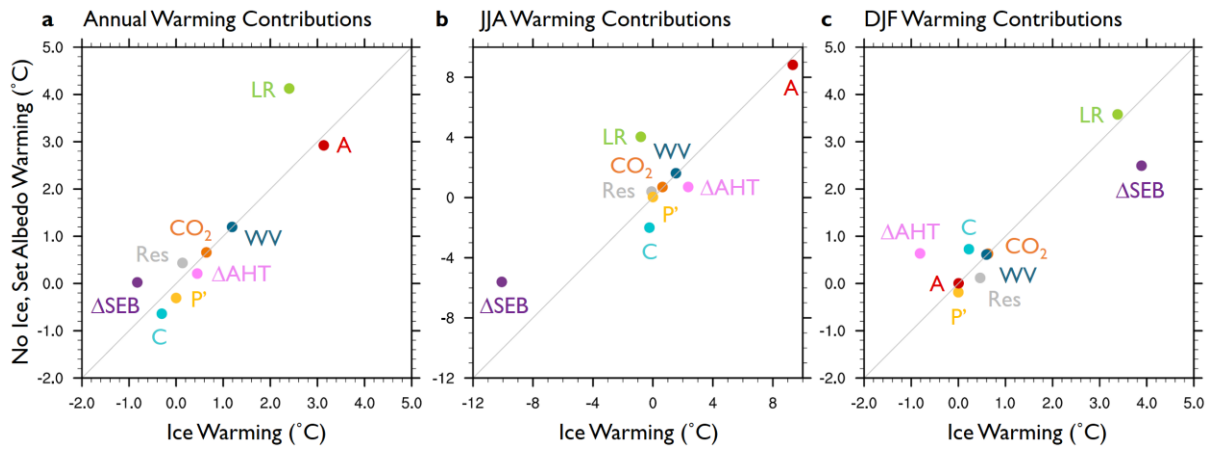
889

890

891

892

893



894

895 **Figure S5.** As in Figure 8, but using October radiative kernels to calculate JJA longwave
 896 feedbacks and using the APRP method to calculate all shortwave feedbacks: contributions to
 897 (a) annual-mean, (b) JJA, and (c) DJF warming ($^{\circ}\text{C}$) over non-land surfaces from $70\text{-}90^{\circ}\text{N}$
 898 under CO_2 doubling in CESM *Ice* and *No ice, set albedo* experiments. Warming contributions
 899 are shown for the lapse-rate (LR), surface albedo (A), water-vapor (WV), and cloud (C)
 900 feedbacks, the variation in the Planck response from its value in the *Ice* experiment (P'), CO_2
 901 forcing (CO_2), change atmospheric heat transport convergence (ΔAHT) and surface energy
 902 budget (ΔSEB), which includes ice export and seasonal ocean heat storage, and residual term
 903 (Res).